LEUPHANA
UNIVERSITÄT LÜNEBURG

Experimentally validated multi-step simulation strategy to predict the fatigue crack propagation rate in residual stress fields after laser shock peening

Keller, S.; Horstmann, M.; Kashaev, N.; Klusemann, B.

Published in:
International Journal of Fatigue

DOI:
10.1016/j.ijfatigue.2018.12.014

Publication date:
2019

Document Version
Publisher's PDF, also known as Version of record

Link to publication

Citation for pulished version (APA):
Keller, S., Horstmann, M., Kashaev, N., & Klusemann, B. (2019). Experimentally validated multi-step simulation strategy to predict the fatigue crack propagation rate in residual stress fields after laser shock peening. *International Journal of Fatigue*, *124*, 265-276. https://doi.org/10.1016/j.ijfatigue.2018.12.014

General rights
Copyright and moral rights for the publications made accessible in the public portal are retained by the authors and/or other copyright owners and it is a condition of accessing publications that users recognise and abide by the legal requirements associated with these rights.

- Users may download and print one copy of any publication from the public portal for the purpose of private study or research.
- You may not further distribute the material or use it for any profit-making activity or commercial gain
- You may freely distribute the URL identifying the publication in the public portal ?

Take down policy
If you believe that this document breaches copyright please contact us providing details, and we will remove access to the work immediately and investigate your claim.

Download date: 04. Dez.. 2025

International Journal of Fatigue 124 (2019) 265–276

Contents lists available at ScienceDirect

International Journal of Fatigue

journal homepage: www.elsevier.com/locate/ijfatigue

Experimentally validated multi-step simulation strategy to predict the fatigue crack propagation rate in residual stress fields after laser shock peening

S. Keller[a,*], M. Horstmann[a], N. Kashaev[a], B. Klusemann[a,b]

[a] Helmholtz-Zentrum Geesthacht, Institute of Materials Research, Materials Mechanics, Department of Joining and Assessment, Max-Planck-Straße 1, 21502 Geesthacht, Germany

[b] Leuphana University of Lüneburg, Institute of Product and Process Innovation, Universitätsallee 1, 21335 Lüneburg, Germany

ARTICLE INFO

Keywords:
Fatigue crack growth
Residual stresses
Numerical simulation
Laser shock peening
Stress intensity factor

ABSTRACT

Laser shock peening (LSP) is a promising technology to retard the fatigue crack propagation (FCP) in metallic lightweight structures. A multi-step simulation strategy to predict FCP in LSP-induced residual stress fields is proposed and applied. The simulation strategy involves an LSP process simulation, a transfer approach to include the plastic strains in a C(T) specimen model to calculate the residual stresses and an FCP simulation to determine the stress intensity factors. The FCP rate is finally determined via FCP equations. The validity of the simulation strategy including the crack driving quantities prediction is experimentally demonstrated by a novel 'simulation' approach.

1. Introduction

For a damage-tolerant design [1], fatigue and corrosion are the two main causes of failure in the aircraft industry [2]. Laser shock peening (LSP) provides a surface treatment that introduces compressive residual stresses with high penetration depth in critical regions susceptible to fatigue phenomena. These compressive residual stresses may lead to the retardation of the fatigue crack propagation (FCP), as shown for M(T) specimens consisting of AA2024-T3 [3] or for friction-stir-welded AA7075-T7351 [4]. However, the generation of compressive residual stresses always causes tensile residual stresses within the structure to keep stress balance. These tensile residual stresses might lead to an acceleration of the FCP rate. Thus, the exact knowledge of the applied residual stress field and the prediction of the resulting FCP rate are necessary to guarantee an effective and optimized application of LSP.

A frequently applied strategy of FCP simulations is to calculate the minimum and maximum stress intensity factors of the fatigue load cycles and to use these stress intensity factors as input for an FCP equation [5–8]. The applied FCP equation links the stress intensity factors at the crack tip to the FCP rate. This work applies the very first FCP equation developed by Paris and Erdogan [9], Walker's equation [10], which was, for example, successfully used within the residual stress field caused by laser heating [11], as well as the NASGRO equation [12], which is nowadays often used to predict FCP rates [5–7]. The different FCP equations are mainly based on the stress intensity factor range and the stress intensity factor ratio R, which can be calculated directly from the minimum and maximum stress intensity factors. The detailed differences between the FCP equations are discussed in the following section.

The literature usually refers to two approaches to predict the stress intensity factor at the crack tip [7]. The first is based on the assumption that crack closure leads to a reduced , determined usually by a crack opening function, as originally proposed by Elber [13], since the stress intensity does not exist for a closed crack. The second frequently used approach is based on stress intensity factors caused by the superposition principle of stress intensity factors caused by the residual stresses and the applied loads [14–16].

Elber [13] was the first to propose a crack opening function f that relates the maximum applied stress intensity factor $K_{appl,max}$ to the stress intensity factor K_{op}, which is needed to open the crack. K_{op} is used to define an effective stress intensity factor range $\Delta K_{eff} = K_{appl,max} - K_{op}$ which is taken as the change of the stress intensity factors at the crack tip. The stress intensity factor ratio R is sometimes set to zero based on the assumption that there is no stress intensity for the minimum load if crack closure occurs [14]. It has to be mentioned that crack closure can also be considered by numerical simulations, instead of proposing a crack opening function [17]. Two problems of the crack closure approach arise as soon as a varying residual stress field is present, as

* Corresponding author.
E-mail address: soeren.keller@hzg.de (S. Keller).

https://doi.org/10.1016/j.ijfatigue.2018.12.014
Received 14 August 2018; Received in revised form 11 December 2018; Accepted 14 December 2018
Available online 16 December 2018
0142-1123/ © 2018 The Authors. Published by Elsevier Ltd. This is an open access article under the CC BY-NC-ND license (http://creativecommons.org/licenses/BY-NC-ND/4.0/).

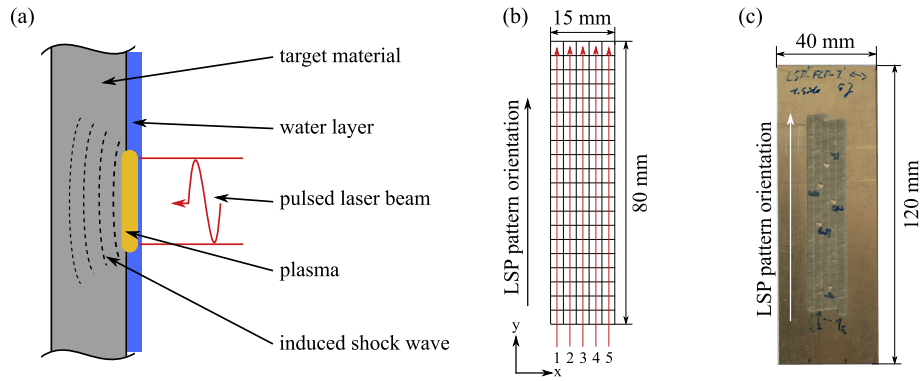

Fig. 1. Scheme of the LSP process (a), the LSP shot pattern (b), and the geometry of the hole drilling (HD) specimens (c). 5 J laser pulses with the full width of half maximum (FWHM) of 20 ns were shot with 10 Hz, without pulse overlap. The LSP pattern was applied twice on each side of the specimens.

caused by LSP [18] or welding [19]. The first, the loading at which crack closure occurs depends strongly on the local residual stresses. Hence, the crack closure function depends strongly on the current position of the crack tip. Therefore, the crack closure function changes with growing crack. However the determination of a crack closure function for every possible residual stress distribution of every crack length is impractical. In the absence of residual stresses, the crack closure depends on the plastic zone at the crack tip [13]. Hence, stress intensity is directly linked to crack closure. This relationship makes the determination of a crack closure function suitable for the base material but not for samples including highly varying residual stresses. The second problem is related to the idea proposed by Elber [13], who took crack closure into account due to plastic deformations resulting from the stress intensity at the crack tip. Hence, crack closure occurs every time at the same position relative to the crack tip, as long as the external loading is kept constant. However, highly varying residual stress fields might cause crack closure not linked to the crack tip. Therefore, the assumption that crack closure reduces the minimum stress intensity factor cannot be made to calculate ΔK_{eff}.

The second approach is based on the idea to superpose the stress intensity factors of the residual and applied stresses to calculate the stress intensity at the crack tip: $K_{tot} = K_{appl} + K_{res}$ [14,15]. Thus, the stress intensity factor is split into an applied and a residual stress intensity factor K_{appl} and K_{res}, respectively, which are traditionally calculated independently of each other. The calculation of K_{appl} and K_{res} can be performed by numerical methods such as the finite element (FE) method. Difficulties occur if the internal force lines caused by the applied loads change depending on the applied force. This leads to nonlinearities, which do not allow the application of the described traditional superposition principle any more. An observed phenomenon that causes such changes in the internal force lines is crack closure. Crack closure is often present in regions of high compressive residual stresses, where the area of crack closure does not have to be connected to the crack tip. Thus, the traditional superposition principle does not seem to be suitable to describe the FCP behaviour after LSP sufficiently. Quantities as inputs for the FCP equations have to be identified. Additionally, an efficient method to calculate these quantities has to be developed to enable an accurate prediction of the FCP rate when significant tensile or compressive residual stresses are present.

In the current study, the aluminium alloy AA2024-T3 is investigated. It is one of the most widely used alloys in manufacturing of metal airframes [20]. The beneficial properties of AA2024-T3 are their very good fatigue crack growth resistance and high fracture toughness. However, AA2024-T3 exhibits a relatively low yield strength [21]. For a detailed review of recent developments in aluminium alloys, the interested reader is referred to Dursun and Soutis [20].

The purpose of this work is the prediction of the FCP rate in spatially highly varying residual stress fields introduced by LSP in AA2024-T3. Therefore, a multi-step simulation strategy is proposed, allowing the prediction of the FCP rate based on the inputs of an LSP process simulation only. For a given geometry and material behaviour, the input parameters of the LSP process simulation are reduced to the pressure acting on the target surface and the laser pulse sequence. The simulation approach is fairly general and can be applied to any residual stress field since it avoids the mentioned limitations. The simulation strategy involves the prediction of the plastic strains after LSP via a process simulation and the transfer of the plastic strains to an FE C(T) specimen to predict the residual stresses, which are used to calculate the crack-driving quantities that are finally applied to FCP equations to predict the FCP rate. Finally, the predicted crack-driving quantities in the peened material were experimentally applied by controlling the external loading to unpeened material to investigate the importance of other influences which might be changed by the LSP treatment, except residual stresses.

2. Theoretical principles and experimental techniques

2.1. Laser shock peening

2.1.1. Short overview about laser shock peening

Laser shock peening is an efficient local modification technique to introduce compressive residual stresses into a workpiece. The effect of laser pulses on a target were first discovered by Askar'yan and Moroz [22] in 1963. Early publications focused on changes in the microstructure and mechanical properties of the material, see e.g. [23]. Peyre et al. [24] studied the ability to increase the performance of different aluminium alloys by applying LSP. An overview of possible surface enhancements based on LSP is given by Clauer and Lahrmann [25]. Residual stresses can also be modified by several alternative techniques such as hammer peening, shot peening, and laser heating, see for an overview Sticchi et al. [26]. However, LSP provides a large penetration depth in combination with a relatively high surface quality [24].

LSP uses short-time (nanosecond) laser pulses to vaporize material next to the target surface, as illustrated in Fig. 1(a). The vaporized material is turned into plasma and expands rapidly due to the heat. This heat expansion generates a surface pressure acting on the target [27]. This surface pressure introduces shock waves into the material, which lead to local plastic deformations. The elastic constraint of the plastically deformed portion results in a residual stress field that is dominated by compressive stresses below the radiated surface. These stresses are balanced by tensile residual stresses in the surrounding volume.

The surface pressure is increased by a transparent overlay, in this work water, which is passed by the laser pulse, but the overlay influences the expansion of the plasma, see e.g. the review of the physics and application of LSP by Peyre and Fabbro [28]. The direct radiation, using only a transparent overlay, might cause tensile residual stresses near

the surface. Based on the investigation of 55C1 steel, Peyre et al. [29] linked these tensile stresses to the heat effects of the plasma. Additionally, the authors showed that these tensile stresses can be avoided using an ablative layer between water and target surface. Such tensile surface stresses are critical for the fatigue crack initiation. However, as this study is focused on the FCP of long cracks, it is expected that such tensile residual stresses at the surface do not influence the present result significantly. Additionally, no ablative (sacrificial) layer is used, to ensure the exact same conditions for every laser pulse, which might be influenced by the interface of an ablative layer and the material otherwise.

Numerical simulations can be used to predict the residual stresses and study the LSP process to arrive at a deeper understanding of the physical mechanisms. However, the simulation of subsequent processes or loadings after the LSP treatment may lead to the discretization of relatively large geometries. Consequently, these relatively large FE models cause a high computational effort for simulating the LSP process, as performed in [30] or [31]. Achintha and Nowell [32] used an approach where plastic strains were predicted in an explicit simulation and then applied as eigenstrains in a second simulation to calculate the residual stresses. In the present study, a similar approach is performed. First, the plastic strains are determined in an explicit finite element simulation of the LSP process. Secondly, the values of the plastic strains are extracted and subsequently introduced into a second, typically much larger, FE model, including an expansion to a larger peened area based on the assumption of periodicity. The assumption of periodicity of the plastic strains is made and justified in Keller et al. [33]. The method to include and expand the LSP-treated area in the second model is not restricted to FCP simulations, as described in Section 3.

Usually, two challenges arise during the process simulation of LSP. The first is the application of the correct plasma pressure which acts at the target surface, while the second is related to the correct modelling of the material behaviour at high strain rates. There are plasma models that allow the prediction of the pressure at the surface, such as the one-dimensional model proposed by Fabbro et al. (1990). Otherwise, the pressure pulse distribution can be identified by fitting the relevant parameter to obtain the desired residual stress profile [33]. Since high strain rates lead to different material responses due to rate-dependant strain hardening and thermal softening caused by heat generation during the plastic deformations [34], a correct description is essential. Amarchinta et al. [34] provided a comparison of different material models used in LSP simulations and stated that the Johnson-Cook model [35] provides consistent results and was in better agreement with experiments than the other investigated material models. Therefore, the Johnson-Cook model is used in this work where the pressure pulse, identified from the residual stress profile, is used from our previous work [33].

2.1.2. Application of laser shock peening

Hole drilling (HD) specimens and C(T) specimens were peened during this study, see Figs. 1(b) and 2, respectively. HD specimens were used to determine the residual stresses, C(T) specimens to investigate the FCP behaviour, see Section 2.4.2. Both HD and C(T) specimens were cut from the same AA2024 sheet with 4.8 mm thickness including an approximately 0.15 mm thick clad layer on both sides. The LSP treatment of HD as well as C(T) specimens is the same as described in the following. An Nd:YAG laser with a 3×3 mm^2 squared laser focus and 5 J laser pulses with the full width of half maximum (FWHM) of 20 ns is used. Based on the FWHM the average laser power intensity is 2.78 GW/cm^2. The laser pulses of each pulse-sequence were placed in the pattern shown in Fig. 1(c). The pattern consists of five columns which are shot consecutively. The processing direction of each column is kept constant during the experiments. The laser beam position is fixed. The specimens were moved with 30 mm/s, while the laser shot frequency was 10 Hz leading to no shot overlap. Synchronization uncertainties between the laser and the robot, which is used to control the position of the specimen, led to slightly varying initial positions (y-coordinate) of the first shot of each column. A relatively large column size of 80 mm is used to equalize these inaccuracies as the fatigue crack is located in the centre of the C(T) specimen. Edge effects, caused by the inaccuracies of the position of the first and last laser shots of each column, are assumed to be negligible, owing to the relatively large distance to the crack tip. No pulse overlap is used in the sequence. However, the sequence was repeated a second time, leading to 100% overlap of the sequences, named in the following two layers of the laser pulse sequence. After the first side of the specimen was processed with both sequence layers, the second side is peened with two sequence layers as well. The LSP treatment and the resulting residual stresses did not lead to significant deformations of the HD specimens with dimensions 40 mm × 120 mm × 4.8 mm as well as of the C(T)-specimens.

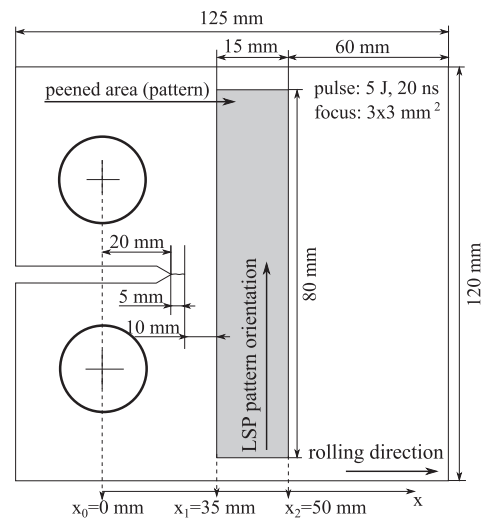

Fig. 2. Geometry of the used C(T) specimen. x_0, x_1, and x_2 are used to partition the specimen in three areas to simplify the discussion of the results, see Section 4. 5 J laser pulses with the full width of half maximum (FWHM) of 20 ns are shot with 10 Hz, without overlapping each other, according to the pattern shown in Fig. 1. Two layers of this laser pulse sequence were shot on both sides of the C(T) specimen.

2.2. Residual stress measurement

The residual stresses were measured using the incremental HD technique with electronic speckle pattern interferometry, described by Steinzig and Ponslet [36–38]. The measurement system Prism from Stresstech is applied, which involves three steps. First, a part of the material, which contains residual stresses, is removed incrementally using a driller. Second, the surface displacements are measured using images before and after the material removal based on electronic speckle pattern interferometry. Third, the stresses, which prevented the surface deformations before the increment was drilled, are calculated for each increment using the integral method [39].

In this work a driller with 2 mm diameter is used. Therefore, the depth of the residual stress measurements is restricted to 1 mm. Residual stresses were measured from both sides of the HD specimens, where the residual stresses of each side were measured at least eight times. Residual stress measurements were placed in the peened area with a certain distance to the borders of the peened area to determine a characteristic residual stress profile. The measured residual stress profile did not show a dependency on the measurement position, which is indicated by the low standard deviation of the measurements.

2.3. Principle of stress intensity factors

The stress intensity factors are usually used to describe the stress state next to a crack tip [40]. Their calculation is based on the

assumption of linear elastic material behaviour. In the following, the definition and consequences resulting from our definitions of the different parts of the stress intensity factors are discussed. The definitions are used to describe the changing stress field next to the crack tip, especially for highly varying residual stresses. It is important to note that other definitions of the decomposition of stress intensity factors are possible, as mentioned in the references listed in Section 1. Similar to the traditional superposition principle, for regions with significant residual stresses the stress intensity factor can be divided into two parts, K^*_{appl} and K^*_{res}.

The first part K^*_{appl} is caused by applied or external loads, while the second part K^*_{res} describes the stress intensity that remains after the removal of all external loads.[1] Therefore, K^*_{res} results only from residual stresses. The stress intensity factor that is present at the crack tip when an applied load and residual stresses are present simultaneously is named K_{cd}.

High residual stresses may lead to significant geometric changes resulting in crack closure effects, for example [17]. These influence the resulting stress distribution next to the crack by changing the internal force lines. Partial crack closure effects can be observed at high compressive residual stresses, where the crack is not completely opened even at certain applied tensile loads. Hence, K^*_{appl} might be different for the same applied load but different compressive residual stresses. Consequently, the authors define K^*_{appl}[2] due to externally applied loads as the difference between K_{cd} and K^*_{res}:

$$K^*_{appl} := K_{cd} - K^*_{res}. \tag{1}$$

In the following, three cases are discussed that explain the consequences of this definition:

2.3.1. Case 1: No residual stresses are present

This is simplified as $K^*_{appl} = K_{cd} = K_{appl}$. Based on linear elastic fracture mechanics, it is possible to find a relationship between the applied load F_{appl} and the stress intensity factor K^*_{appl}, which holds in a certain range of the crack length a, as shown for the standardized C(T) specimens in ASTM E647-11

$$\Delta K_{appl} = \frac{\Delta F_{appl}\left[2+\frac{a}{W}\right]}{B\sqrt{W}\left[1-\frac{a}{W}\right]^{3/2}}\left[0.886 + 4.64\frac{a}{W} - 13.32\left[\frac{a}{W}\right]^2 + 14.72\left[\frac{a}{W}\right]^3 - 5.6\left[\frac{a}{W}\right]^4\right], \tag{2}$$

where W is the length of the C(T)100-specimen, B its thickness, and a is the current crack length.

2.3.2. Case 2: Residual stresses without a change in geometry

In case of residual stresses without a change in geometry, linear elastic fracture mechanics implies that the traditional superposition of K_{appl} and K_{res} is valid, as both can be calculated independently of each other. In case of tensile residual stresses, this leads to $K^*_{appl} = K_{appl}$ and $K^*_{res} = K_{res}$. Case 2 is present when the applied loads cause a completely opened crack. When it comes to compressive residual stresses, K_{res} can be calculated by allowing the penetration of the crack edges based on an FE model, as shown by Schnubel and Huber [17]. This is based on the assumption that the internal force lines in the specimen are not changed.

2.3.3. Case 3: Residual stresses with a change in geometry

The case of geometric changes due to residual stresses is present for large compressive residual stresses, resulting in crack closure. K^*_{appl} and K^*_{res} cannot be calculated independently of each other. This implies that the function that relates an external load F_{appl} to the crack-driving stress intensity factor K_{cd} is influenced by the amount and the position of crack closure.

2.3.4. Definition of the crack driving quantities ΔK_{cd} and R_{cd}

In this work, stress intensity factors are used to describe the changing stress field in front of a fatigue crack caused by cyclic loading. In this regard, the authors introduce the ratio R_{cd} of the minimum $K_{cd,min}$ and maximum $K_{cd,max}$ crack-driving stress intensity factors, as well as the crack-driving stress intensity factor range ΔK_{cd} as

$$R_{cd} = \frac{K_{cd,min}}{K_{cd,max}}, \quad \Delta K_{cd} = K_{cd,max} - K_{cd,min}. \tag{3}$$

It is important to mention that R_{cd} differs from the ratio of the applied loads R_{Load} in Cases 2 and 3, which is for a C(T) specimen calculated as

$$R_{Load} = \frac{F_{appl,min}}{F_{appl,max}}. \tag{4}$$

$F_{appl,min}$ and are the minimum and maximum applied forces. Considering Case 1, the crack-driving stress intensity factor ratio R_{cd} corresponds to the applied load ratio R_{Load}.

2.4. Fatigue crack propagation

2.4.1. Fatigue crack propagation equations

FCP equations were developed to relate stress intensity factors as quantities of fracture mechanics to the FCP rate. It is assumed in this study that the introduced FCP equations are applicable in areas of significant residual stresses, as long as the crack-driving quantities (ΔK_{cd} and R_{cd}), describing the stress intensity at the crack tip, are used. Paris and Erdogan [9] established the first FCP equation $\mathrm{d}a/\mathrm{d}N = f(\Delta K_{cd})$, where the FCP rate $\mathrm{d}a/\mathrm{d}N$ is a function of the stress intensity factor range ΔK_{cd} only:

$$\mathrm{d}a/\mathrm{d}N = C_P\,\Delta K_{cd}^{n_P}, \tag{5}$$

where C_P and n_P are material parameters of Paris's law. Nowadays, several crack growth laws are used which consider additional quantities, such as the ratio R_{cd} of the minimum and maximum stress intensity factor, the threshold stress intensity factor range ΔK_{th}, and the fracture toughness K_c. While R_{cd}, in addition to ΔK_{cd}, is used to describe the mean stress effect on $\mathrm{d}a/\mathrm{d}N$, ΔK_{th} and ΔK_c enable the prediction of $\mathrm{d}a/\mathrm{d}N$ in the threshold and fracture toughness regime. A frequently used FCP equation that takes these quantities into account is the NASGRO equation

$$\frac{\mathrm{d}a}{\mathrm{d}N} = C_{NA}\left[\Delta K_{cd}\frac{[1-f_N]}{[1-R_{cd}]}\right]^{n_{NA}}\frac{\left[1-\frac{\Delta K_{th}}{\Delta K_{cd}}\right]^p}{\left[1-\frac{K_{cd,max}}{K_c}\right]^q}, \tag{6}$$

where C_{NA}, n_{NA}, p, and q are material parameters. $K_{cd,max}$ is the maximum stress intensity factor at the crack tip. f_N is the crack opening function determined by Newman [41]

$$f_N = \frac{S_o}{S_{max}} = A_0 + A_1 R + A_2 R^2 + A_3 R^3 \quad \text{for} \quad R \geqslant 0, \tag{7}$$

where the coefficients $A_i = g(K_{max}, \sigma_Y, \alpha)$ depend on the maximum stress intensity factor K_{max}, the yield strength σ_Y, and a constant α, which is 1 for a plane stress or 3 for a plane strain state. The crack opening function is used to consider crack closure, caused by the plastic wake behind the crack tip. The plastic wake results from plastic deformation at the crack tip.[3] This study considers load cases above the threshold region and below the region that is influenced by the fracture

[1] K^*_{res} is calculated with consideration of crack closure effects.

[2] K_{appl} is traditionally used as a stress intensity factor caused by the applied load without residual stresses or crack closure effects.

[3] This work does not consider the change in the plastic wake which may result from present residual stresses. Hence, plastic deformations and residual stresses, which are generated by the stress intensity at the crack tip itself, are not included in the following simulations, see Section 3.

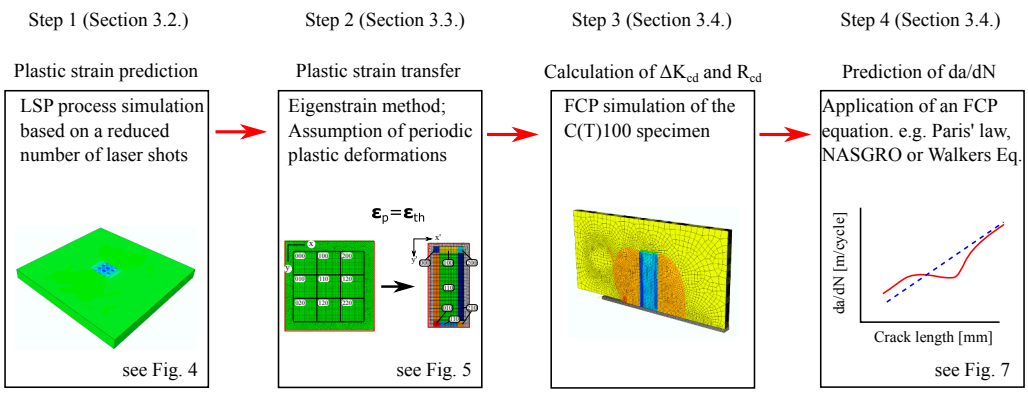

Fig. 3. Multi-step simulation approach comprising four steps. Step 1 represents the determination of the plastic strains using an LSP process simulation based on a reduced number of laser impacts. These plastic strains are transferred to the following FCP simulation based on the eigenstrain method, Step 2. Step 3 deals with the calculation of ΔK_{cd} and R_{cd} on the basis of the FCP simulation, which are used as inputs for the FCP equations in Step 4.

toughness. Therefore, the NASGRO equation can be reduced to

$$\frac{da}{dN} = C_{NA}\left[\Delta K_{cd}\frac{[1-f_N]}{[1-R_{cd}]}\right]^{n_{NA}}. \tag{8}$$

Facing the challenge of the FCP prediction in regions with significant residual stresses, Schnubel and Huber [11] used Walker's equation [10]

$$\frac{da}{dN} = C_W\left[\frac{\Delta K_{cd}}{[1-R_{cd}]^{1-m}}\right]^{n_W}, \tag{9}$$

to calculate the FCP rate. As Schnubel and Huber [11] achieved good agreements between experiments and simulations for the FCP rate prediction in residual stress-dominated regimes, Walker's equation is considered in this work as well.

2.4.2. Fatigue crack propagation test

The FCP experiments were performed according to ASTM standard using C(T)100 specimens. The specimen geometry is shown in Fig. 2. The applied load ratio R_{Load} was kept constant during the experiments. The specimens were 5 mm pre-cracked leading to an initial crack length of 25 mm to avoid influences of the manufacturing process of the initial notch, and the crack initiation at the beginning of the FCP test. The LSP process was applied after the pre-cracking, see Section 2.1.1. Unpeened specimens were tested at the load ratios: $R_{Load} = 0.1$ with $F_{appl,max} = 4$ kN and $F_{appl,min} = 0.4$ kN (three repetitions), as well as $R_{Load} = 0.7$ with $F_{appl,max} = 4$ kN and $F_{appl,min} = 2.8$ kN (two repetitions). Peened specimens were tested with the load ratio of $R_{Load} = 0.1$ (three repetitions).

3. Multi-step simulation to predict the FCP-rate

3.1. Multi-step simulation approach

The aim of the proposed multi-step simulation approach is the prediction of the FCP rate influenced by residual stresses based on the LSP treatment. The prediction of the FCP rate is realized by the following sequence of four steps, as illustrated in Fig. 3:

1. An LSP process simulation predicts the plastic strains after LSP treatment, following the approach presented in Keller et al. [33].[4]
2. Plastic strain transfer from the LSP process model to a crack extension model (e.g. C(T) specimen) using the eigenstrain method to predict the residual stresses [42].[5]
3. FCP simulation to calculate ΔK_{cd} and R_{cd} for certain crack lengths.
4. Application of an FCP equation to determine the crack growth rate da/dN.

3.2. Step 1: LSP process simulation

Plastic strains are predicted based on the LSP nine-shot model developed in [33] for AA2198, see Fig. 4. The plasma pressure is modelled as pressure loading acting on the surface. The adjusted pressure pulse for 5 J and 20 ns (FWHM) with a square 3 × 3 mm² laser focus from [33] is used. The pressure pulse adjustment is performed by fitting numerically predicted residual stresses to the measurements for AA2198-T3. In [33], this pressure pulse is applied subsequently to AA2198-T8. In addition, the pressure pulse were scaled and applied to the focus size of 1 × 1 mm² for AA2198-T3 and AA2024-T8. As the measured and predicted residual stresses agree well, it was concluded that the adjusted pressure pulse produces physical residual stresses and plastic strains considering the applied averaging scheme in the numerical model as well as in the experimental incremental hole drilling method. However, the adjusted pressure pulse does not to be the physical correct plasma pressure, it is only sufficient to predict the correct plastic strains as needed in this work. An FE model consisting of continuum elements with reduced integration (C3D8R) is built and solved using ABAQUS, see Fig. 5. Fixed boundary conditions are used at the boundaries of the modelled material sheet on x-z and y-z planes. The top and bottom surfaces (parallel to the x-y plane) of the specimen are modelled as free surfaces. The model size is 60 × 60 × 4.8 mm³. An element size of approximately 0.15 × 0.15 × 0.02 mm³ is used to provide a mesh-independent solution at the surface. The strain rate-dependent yield stress σ_Y is determined with the reduced Johnson-Cook model [35]

$$\sigma_Y = [A_{JC} + B_{JC}\,\varepsilon_p^{n_{JC}}]\left[1 + C_{JC}\,ln\left[\frac{\dot{\varepsilon}_p}{\dot{\varepsilon}_{p,0}}\right]\right], \tag{10}$$

where ε_p is the plastic strain and $\dot{\varepsilon}_p$ the plastic strain rate. A_{JC}, B_{JC}, C_{JC} and n_{JC} are material parameters. Temperature effects are neglected. The material parameters for AA2024-T3 are taken from [44] and summarized in Table 1. Simulations showed, that the clad layer does not have a significant impact on the residual stresses through the thickness as the clad layer influences the residual stresses close to the surface only. Therefore, the influence of the clad layer is neglected in the following.

The basic assumption of the LSP nine-shot model is applicability of the principle of periodicity for the resulting plastic strains. Therefore, plastic strains can be predicted by the simulation of a small area that is representative of the larger area of the laser pulse pattern. For the LSP process parameters used by Keller et al. [33], in combination with the investigated material AA2198-T3, a square of 3 × 3 pressure pulses is sufficient to predict the plastic strains below the area which is radiated by the centred laser pulse. This assumption requires that plastic strains

[4] It is important to mention that any source (experimental or simulative) that provides the plastic strains can be used as input for the following steps.

[5] Step 2 can be replaced with any other method that introduces residual stresses into the FCP model (e.g. initial stress method [43]). Hence, measured residual stresses can be introduced into the FCP model as well.

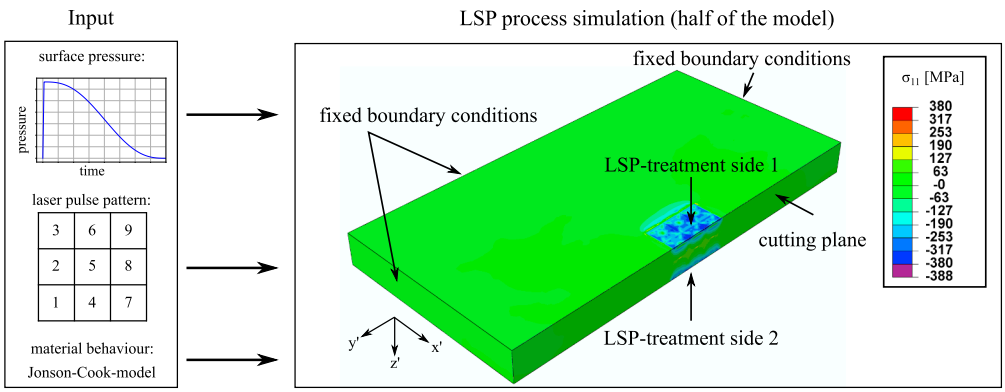

Fig. 4. Half of the LSP process simulation model for the double-sided LSP treatment with two layers of the laser pulse sequence. The LSP process simulation takes the plasma pressure acting at the surface, the laser pulse pattern, and the material behaviour as inputs. The plasma pressure, which is taken from Keller et al. [33], is assumed to be a function of time only. The shown laser pulse sequence is shot twice on both sides. The rate-dependant material behaviour is modelled with the Johnson-Cook model, see Eq. (10).

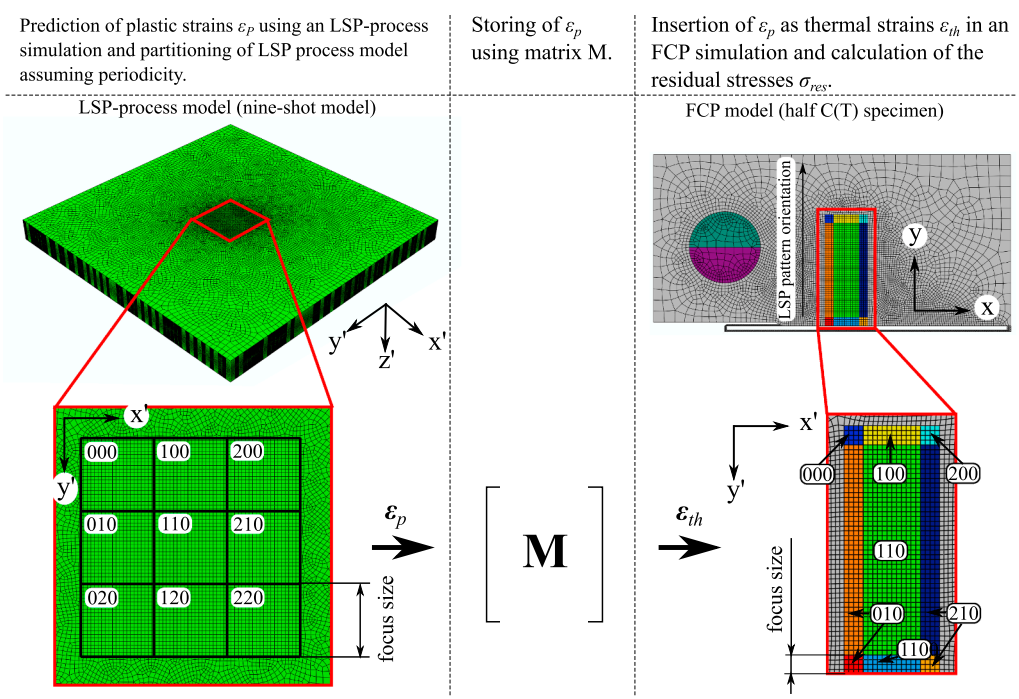

Fig. 5. Eigenstrain approach to introduce residual stresses in the FE model of the C(T) specimen. The LSP process simulation accounts only for the minimum number of laser pulse impacts and contains a volume in which the plastic strains are representative for the specific LSP pattern. The simulated LSP specimen is sliced into volumes in which the plastic strain components $\varepsilon_{p,ij}$ are averaged and then stored in a matrix M. The FCP model is sliced into volumes as well. Every volume of the FCP model is assigned to one volume of the LSP process simulation according to its position. $\varepsilon_{p,ij}$ is applied to the FCP model as thermal strains $\varepsilon_{th,ij}$. To apply $\varepsilon_{th,ij}$, the thermal expansion coefficients are calculated and the temperature is raised by a certain ΔT, leading to the desired residual stresses in the FCP simulation.

Table 1
Material parameters of the Johnson-Cook model for AA2024-T3, taken from [44].

Density ρ, g/cm^3	Young's modulus E, MPa	Poisson's ratio, ν	Yield strength A_{JC}, MPa	Strain rate coefficient C_{JC}	Strain hardening exponet n_{JC}	Strength coefficient B_{JC}, MPa	Reference strain rate $\dot{\varepsilon}_{p,0}$, s^{-1}
2.78	74326	0.33	350	0.01	0.73	972	0.0002

within the representative area are not influenced by pressure pulses outside the 3 × 3 pressure pulse square. To predict the plastic strains after two-sided LSP treatment of the C(T) specimen, a square of 3 × 3 pressure pulses is applied on both sides of the plate. Each square of 3 × 3 pressure pulses is shot twice, which corresponds to two layers of the sequence. Hence, 36 laser shots need to be simulated. This marks a massive reduction in the number of shots compared to the real LSP experiment, where approximately 530 laser pulses are applied to the C(T) specimen.

3.3. Step 2: Plastic strain transfer and residual stress prediction

The eigenstrain method [42] is used to transfer plastic strains from the LSP process simulation to the subsequent FCP simulation. The transfer of the plastic strains can be performed by the following three main steps. The overall structure of this approach is shown in Fig. 5.

2.1 The LSP process model is partitioned into volumes of size 3 × 3 × 0.2 mm^3, where 0.2 mm represents the depth in z-direction, see Fig. 5. The area in the x-y plane corresponds to the focus size of the laser. The different plastic strain components are averaged in the corresponding volumes and stored using matrix M.

2.2 The region of the FCP simulation, which would contain plastic strains after the LSP treatment, is also partitioned into volumes related to the LSP simulation. These volumes are linked to certain thermal expansion coefficients considering the principle of

periodicity of the plastic strain field caused by LSP.[6] The thermal expansion coefficients are determined by the matrix M of the averaged plastic strains obtained in Step 1. The size of the overall plastically deformed area is manually restricted by the boarders of the peened area within the LSP simulation.

2.3 In an FE simulation of the C(T) specimen, the temperature is increased by a certain ΔT. The different thermal expansions of the partitioned region lead to elastic strains that cause the intended residual stress distribution.

The applied strain averaging scheme neglects local variations of the plastic strains and residual stresses, signifying a strong simplification. The size of the volumes in which the plastic strains are averaged can be reduced to obtain a higher resolution of the residual stress field. However, the observed variations were assumed to be negligible for the FCP behaviour. This was confirmed by the FCP simulations, showing for the used volume a good correlation between experiment and simulation, see Section 4.2. Hence, the chosen volume size is assumed as sufficiently large for the purpose of this work.

3.4. Step 3: FCP simulation to calculate the stress intensity factors

The stress intensity factor K_{cd} is calculated by FE simulations for certain crack lengths. Owing to the symmetric nature of the problem, half of the C(T) specimen is only modelled with symmetry boundary conditions on the symmetry plane, see Fig. 5. ABAQUS is used to perform the FCP simulation. Depending on the crack length, the symmetry boundary conditions are replaced by contact conditions to a rigid plate with no friction in x- and z-direction. The contact to the rigid plate simulates the contact of the crack surfaces.

The crack tip is assumed to be a straight line perpendicular to the specimen surface. In addition, the crack edges are assumed to be a plane that allows the application of symmetry. These assumptions are made for simplicity.

The bolt and the C(T) specimen are modelled as one part to avoid contact in the simulation. A distributed force is applied at the centred nodes of the bolt. To ensure realistic pin loading conditions, the upper part of the bolt contains a high elastic modulus, while the elastic modulus of the lower part is extremely small.

The crack closure technique (CCT) (or crack closure method/two-step crack closure technique) [45] is used to calculate K_{cd} at the crack tip. In the CCT, the energy release rate G is linked to the stress intensity factor K for plane stress conditions, as follows

$$K = \sqrt{G\,E} \quad \text{(plane stress)}. \tag{11}$$

G can be approximately calculated based on an FE simulation and the finite crack extension Δa:

$$G = \frac{1}{2B\,\Delta a}\sum_{i=1}^{N} F_y^i\,u_y^i. \tag{12}$$

B is the thickness of the material sheet and u_y^i are the nodal displacements in y-direction of the used C(T) model. F_y^i are reaction forces at the nodes which are located at the crack tip. The number of nodes at the one-dimensional crack tip is N. To calculate G, the CCT uses the force at each crack tip node before the release of the symmetry boundary condition and the node displacement after its release. Hence, each pair F_y^i and u_y^i is determined at the same node, for which two simulation steps are needed. A similar method to determine G is the virtual (or modified) crack closure technique (VCCT) [45] that uses the displacement of the released nodes next to the crack tip and the force at the crack tip nodes to calculate K. Thus, F_y is determined at the crack tip but u_y is taken from the first node behind the crack tip. VCCT enables the prediction of K in one simulation step at a certain crack length and is supposed to be faster than CCT. In this work, both simulation techniques were compared. From the performed simulations, it was concluded that CCT is less mesh-dependent and thus more suitable for the FCP simulation with the present residual stress distribution in this study. The assumption of similar stress conditions of adjacent nodes is not fulfilled for reasonable mesh sizes in the VCCT due to the high residual stress gradients at the boundaries of the peened area. However, for instance, [7,8] showed the applicability of the VCCT in regions of high residual stresses. For further details regarding the CCT and VCCT, see Krueger [45].

3.5. Step 4: Prediction of the FCP-rate

Prediction of the FCP rate $\mathrm{d}a/\mathrm{d}N$ based on the calculated ΔK_{cd} and R_{cd} using FCP equation (see Table 2), as described in Section 2.4.

4. Results and discussion

4.1. Validation of the eigenstrain method to predict residual stresses in large areas

The eigenstrain approach is validated by a comparison of measured and predicted residual stresses for a C(T) specimen. Fig. 6(a) shows the measured residual stresses in comparison with the residual stresses within the representative area of the LSP process model. Stresses of the LSP process model were averaged to enable comparison with the measured residual stresses according to the averaging scheme in [33]. The averaged stress and the standard deviation of the data points which are considered for the averaging are shown. The standard deviations indicate the high fluctuation of the residual stresses after the LSP process in the direction of the surface plane. Residual stresses were measured using the HD specimens, as described in Section 2.1.2. The simulated and measured residual stresses show a good agreement for σ_{xx}. However, the LSP process model does not show the non-equibiaxiality of the experimentally measured residual stresses in the HD specimen. This non-equibiaxiality can be predicted by the extension of the plastic strains to a larger area, as performed during the transfer from the LSP process model to the C(T) specimen, see Fig. 6(b). The good agreement, especially regarding the non-equibiaxiality of the predicted residual stresses after the eigenstrain method is applied, validates the applicability of the eigenstrain approach and the assumption of the periodicity of the plastic strains. The change from an equibiaxial residual stress field after a simplified LSP process simulation to a non-equibiaxial residual stress field after the eigenstrain approach indicates the importance of the geometry along the overall residual stress distribution.

Residual stresses after the plastic strain transfer based on the eigenstrain method do not show the high spatial fluctuations parallel to the surface as calculated by the LSP process simulation. Hence, the eigenstrain method neglects the fluctuations of the residual stresses in surface plane direction, which is indicated by the decreased standard deviation after the application of the eigenstrain method, while the same averaging scheme is used to enable the comparison to the experiments. Neglected residual stress gradients after the eigenstrain method result from the averaging of the highly fluctuating plastic strains near the surface in the LSP process model. But the residual stress resolution in depth direction (z-direction) is similar to the LSP process simulation. The simulations in the following sections are based on the assumption that the high fluctuations of the residual stress field parallel to the surface do not have a major influence on the FCP behaviour. As mentioned before, the resolution could be increased by a refinement of the segmentation of the LSP process model.

[6] The corner volumes of the LSP simulation are linked to the corner volumes of the FCP simulation and the centre volumes of the LSP simulation are linked to the centre volumes of the FCP simulation, as indicated by the different numbers/colours in Fig. 5.

Table 2
FCP equations for corresponding input parameters see Table 3.

Paris' law [9]	$\frac{da}{dN} = C\Delta K_{cd}^{n}$	• Input parameter ΔK_{cd} • Basic equation to describe FCP
Walker's Eq. [10]	$\frac{da}{dN} = C\left[\frac{\Delta K_{cd}}{(1-R_{cd})^{1-m}}\right]^{n}$	• Input parameters ΔK_{cd} and ΔR_{cd} • Consideration of the mean-stress effect
NASGRO Eq. [12]	$\frac{da}{dN} = C\left[\Delta K_{cd}\frac{(1-f_N)}{(1-R_{cd})}\right]^{n}$	• Input parameters ΔK_{cd} and ΔR_{cd} • Consideration of the mean-stress effect • Inclusion of a crack opening function • Assumption of plane stress state

Table 3
Parameters of different fatigue crack propagation equations. C, n and m are identified based on FCP experiments on unpeened specimens, and α is chosen depending on the stress state of a relatively thick specimen.

Material parameters	C	n	m	α	σ_Y [MPa]
Paris' law, Eq. (5)	$1.369\cdot10^{-10}$	3.019	–	–	–
Walkers equation, Eq. (9)	$4.309\cdot10^{-11}$	3.394	0.866	–	–
NASGRO equation, Eq. (8)	$4.435\cdot10^{-11}$	3.646	–	3.0[a]	350

[a] Taking α as a variable with $\alpha \in [1.0, 3.0]$ during the parameter identification leads to $\alpha = 3.0$. $\alpha = 3.0$ is reasonable since it corresponds to a plane stress state.

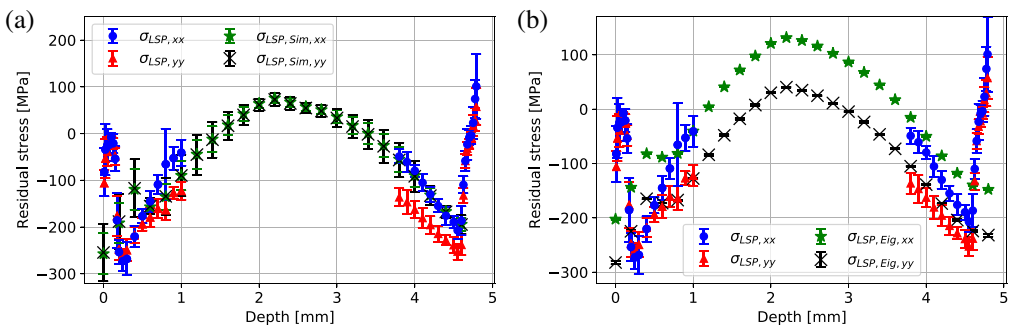

Fig. 6. Residual stresses of the LSP process simulation (a) and predicted residual stresses after the eigenstrain approach (b) compared to experimentally measured residual stresses for the HD specimen. Results of the simulation show the averaged residual stresses and the standard deviation in the averaging volume, as explained in Keller et al. [33]. The residual stresses of the LSP process model prediction (a) show the standard deviation of all points involved in the averaging scheme. The good agreement of the predicted residual stresses, especially regarding the non-equibiaxiality of the residual stresses after the transfer of the plastic strain to the C(T) specimen (b), validates the eigenstrain approach to extend residual stresses to large areas.

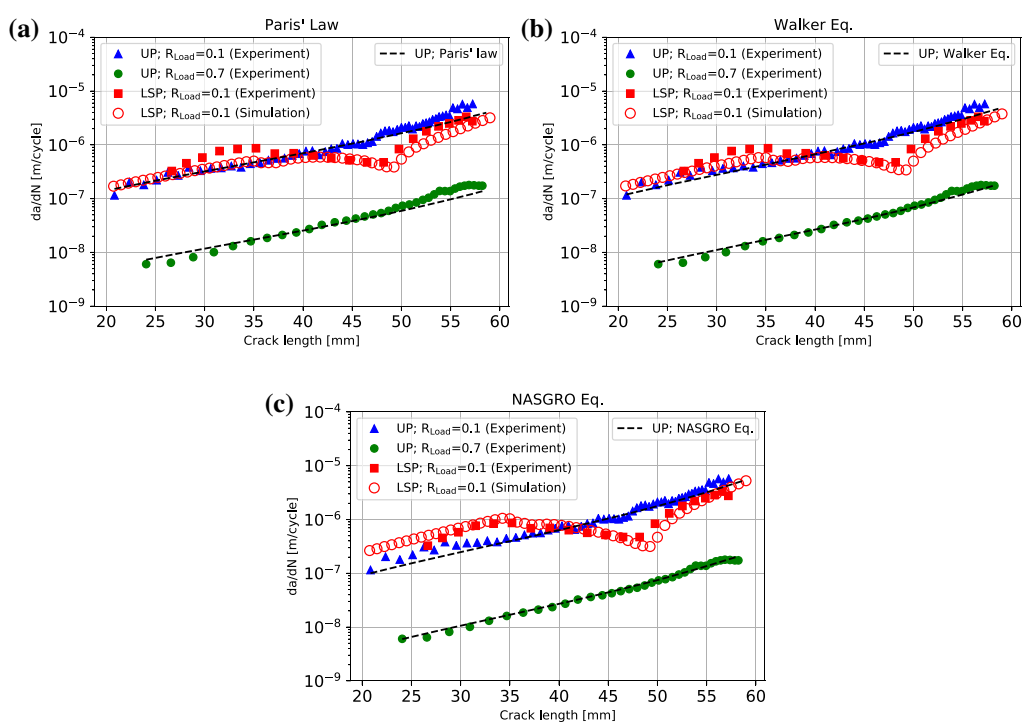

Fig. 7. Measured FCP rates of unpeened (UP) specimens for $R_{Load} = 0.1$ and $R_{Load} = 0.7$ are used to identify material parameters of the FCP equations: (a) Paris's Law (5), (b) Walker's Eq. (9), and (c) the NASGRO Eq. (8), see Table 3. Prediction of the FCP rate of laser shock peened specimens (LSP) based on the different FCP equations show differences, especially in front of the peened area (crack length<35 mm). The best agreement between measured and simulated FCP rate for peened specimens is achieved for the NASGRO equation.

4.2. Prediction of the fatigue crack propagation rate da/dN

Material constants of the different FCP equations, i.e. Paris's law (5), NASGRO Eq. (8), and Walker's Eq. (9) are identified using a least square fit to the experimental data for unpeened C(T) specimens for two applied load ratios $R_{Load} = 0.1$ and $R_{Load} = 0.7$, as shown in Fig. 7. Fig. 7 displays representative measurements, where each measurement is repeated at least twice. The identification process of the material parameters uses a running average scheme that prevents inaccuracies due to a non-evenly spaced distribution of the measured values. Experimental information between the crack lengths $a = 28$ mm and $a = 57$ mm are considered for the parameter identification to avoid any influence of running-in phenomena. Additionally, the optical measurement of the crack length for $a > 57$ mm might not be as accurate as for smaller cracks due to the increasing FCP rate. The identified material parameters for the FCP equations are summarized in Table 3, which are in a reasonable range compared to values reported in the literature (e.g. see for Paris's law parameters [46]).

Fig. 7 shows measured and calculated FCP-rates da/dN based in the different FCP equations. The agreement to the experimental data of the unpeened material is slightly better for Walker's and the NASGRO equation, as Paris's law does not consider the mean stress effect.

The agreement of the predicted and measured da/dN values for the peened specimens differs between 25 mm and 40 mm for the different FCP equations, see Fig. 7. As the NASGRO equation provides the most precise predictions of da/dN for $25\,\text{mm} < a < 40\,\text{mm}$, it is recommended for following investigations. A similar observation for butt joints is reported by Servetti and Zhang [7], who concluded that the NASGRO equation gives a better prediction than Walker's equation does for the entire length of the crack, as the NASGRO equation contains more 'fitting' constants.

4.3. Evolution of ΔK_{cd} and R_{cd}

The stress intensity factor at the crack tip of the C(T) specimen for the minimum and maximum applied load, $F_{appl,min}$ and with (peened) and without (unpeened) residual stresses are shown in Fig. 8(a). $K_{cd,min}$ and $K_{cd,max}$ were calculated with the proposed simulation strategy for peened specimen and according to ASTM E647-11 for the unpeened specimen. Unpeened specimens correspond to Case I, where $K_{cd} = K^*_{appl} = K_{appl}$, see Section 2.3. However, the applied stress intensity factor is influenced by residual stresses, as K^*_{appl} of the peened specimen differs from K_{appl} of the unpeened specimen for $a > x_1$, see Fig. 8(b). R_{cd} and ΔK_{cd} of the peened specimens were calculated based on the FE simulations as described in Section 3.4, see Fig. 8(c) and (d). ΔK_{cd} of the peened specimens corresponds to ΔK_{cd} of the unpeened specimen, for $a < x_1$. Thus, the traditional superposition of K_{appl} and K_{res} can be assumed in front of the peened area, which corresponds to Case II, see Section 2.3. This leads to a shift in the stress intensity factor for the peened specimen, resulting in a higher mean stress intensity factor. The increased crack-driving stress intensity factor ratio and the unchanged crack-driving stress intensity factor range compared to the unpeened material indicates this increased mean stress intensity factor, see Fig. 8(c) and (d). While R_{cd} varies depending on the residual stress

$$R_{cd} = [K^*_{appl,min} + K^*_{res}]/[K^*_{appl,max} + K^*_{res}], \tag{13}$$

ΔK_{cd} is not influenced by the residual stresses:

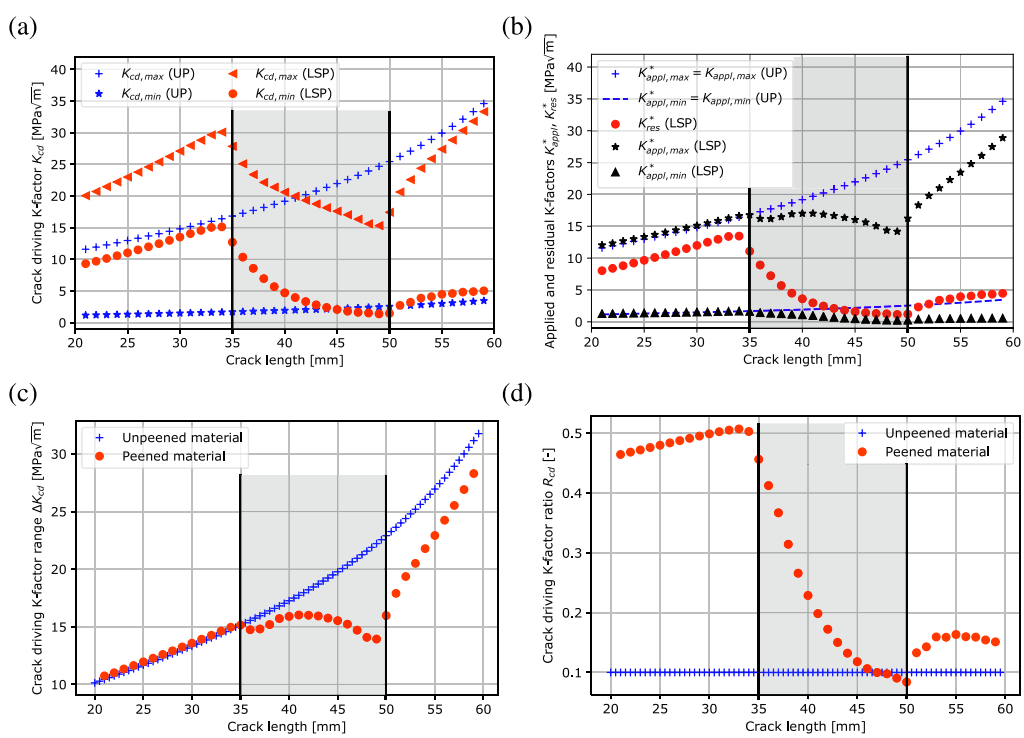

Fig. 8. Prediction of the crack-driving stress intensity factor K_{cd} using FE simulations and linear elastic fracture mechanics. The position of the peened area is marked in grey. (a) Comparison between the minimum and maximum crack-driving stress intensity factor $K_{cd,min}$ and $K_{cd,max}$ of an unpeened (UP) and peened (LSP) specimen. K_{cd} of the unpeened specimen corresponds to the applied stress intensity factor K_{appl} and is calculated based on equations following ASTM E647-11. The applied stress intensity factor of the peened specimen corresponds to the applied stress intensity factor of the unpeened specimen resulting in $K^*_{appl} = K_{appl}$ for $a < x_1$ (b). However, the comparison of K^*_{appl} of peened and unpeened specimens for $a > x_1$ shows, that K^*_{appl} can be different for the same applied loads according to Eq. (1), as K^*_{appl} depends on crack closure effects which are influenced by the residual stress state. The resulting crack-driving stress intensity factor range ΔK_{cd} of the peened specimen corresponds to ΔK_{appl} of the unpeened specimen for $a < x_1$, indicating a pure superposition of the residual and applied stresses (c). However, R_{cd} of the peened specimen is significantly higher than R_{cd} of the unpeened specimen (d).

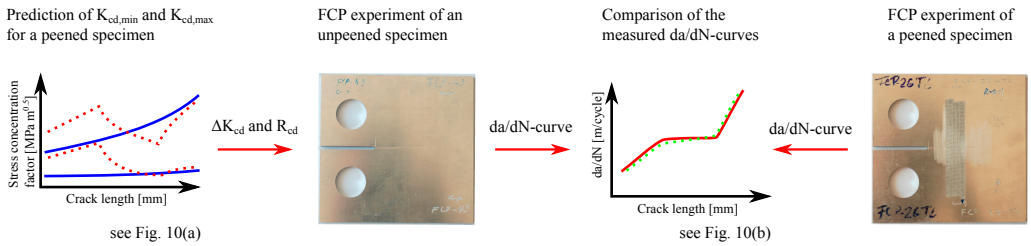

Fig. 9. Validation strategy for the assumed dominant crack-driving quantities ΔK_{cd} and R_{cd} by applying the numerically obtained values to an unpeened specimen using a step-wise constant amplitude loading during an FCP experiment (green dots). The measured $\mathrm{d}a/\mathrm{d}N$-curve is compared with the result of an FCP experiment using a peened specimen (red line) under constant amplitude loading. (For interpretation of the references to colour in this figure legend, the reader is referred to the web version of this article.)

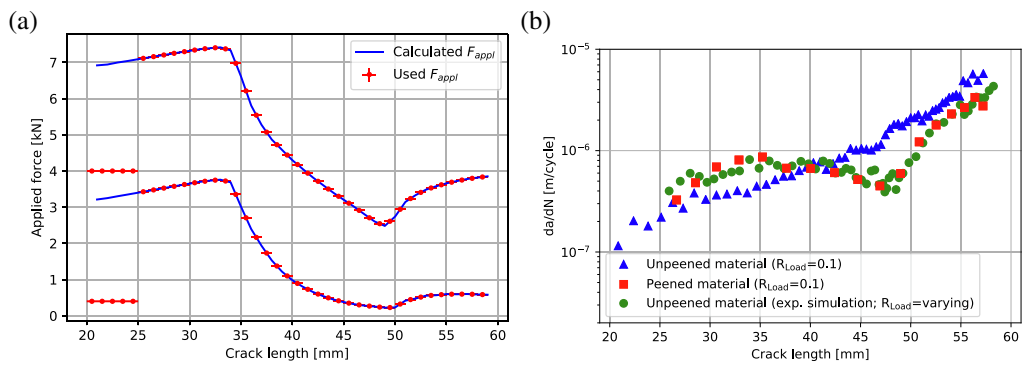

Fig. 10. 'Experimental LSP simulation' using an unpeened specimen. (a) Applied maximum and minimum forces, which are designed to reproduce the numerical predicted ΔK_{cd} and R_{cd} of a peened specimen in an unpeened specimen. The forces were changed step by step during the experiment (constant force intervals, shown here by the red lines). The pre-cracking is considered for 20 mm $< a <$ 25 mm during the 'experimental LSP simulation'. (b) Resulting $\mathrm{d}a/\mathrm{d}N$ curves for the unpeened and peened materials, as well as the 'experimental LSP simulation'. The excellent agreement indicates that ΔK_{cd} and R_{cd} are the main crack-driving quantities. (For interpretation of the references to colour in this figure legend, the reader is referred to the web version of this article.)

$$\Delta K_{cd} = K^*_{appl,max} + K^*_{res} - [K^*_{appl,min} + K^*_{res}] = K^*_{appl,max} - K^*_{appl,min}, \quad (14)$$

as illustrated in Fig. 8(c).[7] The crack growth rate increased with increasing R_{cd} according to the different FCP-equations, see Fig. 7(b) and (c). Since R_{cd} is differently considered in the FCP equations, the different performances to predict $\mathrm{d}a/\mathrm{d}N$ can be explained. Paris's law, for instance, does not contain a mean stress effect, which is why $\mathrm{d}a/\mathrm{d}N$ is predicted as unchanged compared to the unpeened specimen, see Fig. 7(a). Within and behind the peened area, R_{cd} drops significantly to a lower level. Additionally, ΔK_{cd} decreases compared to the unpeened specimen. The influence of the changed ΔK_{cd} dominates $\mathrm{d}a/\mathrm{d}N$ for $a > x_1$. Thus, all FCP equations predict similar $\mathrm{d}a/\mathrm{d}N$-values, see Fig. 7. Inside and behind the peened area ($a > x_1$), the traditional superposition is not valid any more. A detailed discussion about the retardation mechanisms, in particular the effect of crack closure, will be provided in a subsequent publication.

5. Theory validation by experimental LSP simulation

In this study, the FCP-influencing factors are reduced to LSP-induced residual stresses and specimen geometry, which influence the stress distribution within the specimen. Even the crack tip geometry and the effect of the residual stresses are simplified. Owing to the calculation of ΔK_{cd} and R_{cd} for a straight crack tip and plane crack edges, ΔK_{cd} and R_{cd} correspond to thickness averages. The error, which might result from these simplifications and the neglect of unknown effects, could counteract and cover possible errors in the prediction of ΔK_{cd} and R_{cd} as well as $\mathrm{d}a/\mathrm{d}N$. Therefore, the interaction of the residual stresses and the applied loads is experimentally simulated for unpeened specimens by the following procedure, see Fig. 9.

Numerically predicted ΔK_{cd} and R_{cd} values, as determined in Section 4.2, are experimentally applied to an unpeened C(T) specimen by controlling F_{appl}. and $F_{appl,min}$ are calculated by Eq. (2) for certain ΔK_{cd} and R_{cd}. As the experimental set-up does not allow a continuous variation of and $F_{appl,min}$, the forces are changed step by step for every crack length increment of 1 mm. Fig. 10(a) shows the calculated and $F_{appl,min}$, as well as the experimentally applied step-wise constant forces. This approach is named 'experimental LSP simulation' in the following.

In Fig. 10(b) the FCP rate $\mathrm{d}a/\mathrm{d}N$ depending on the crack length a is illustrated for the 'experimental LSP simulation'. This experiment is repeated three times. As the measurements indicate just a small scatter only one representative curve is shown in Fig. 10(b). The 'experimental LSP simulation' of the unpeened material is in good agreement with the experimentally determined FCP rate of the peened material for a crack length in range 25 mm $< a <$ 40 mm, and in excellent agreement for 40 mm $\leqslant a <$ 60 mm. The applied loads of the fatigue experiment had to be reduced to certain static loads after every load interval to change the forces. After the experiment is continued with the changed loads, running-in effects might occur and lead to the 'zigzag' shape of the FCP rate for high applied loads, as seen for 25 mm $< a <$ 35 mm. Such running-in effects lead to an underestimation of the FCP rate, which explains the slightly better agreement for 40 mm $\leqslant a <$ 60 mm.

The high applied load for 25 mm $< a <$ 35 mm leads to an increased plastic zone in front of the crack tip. The influence of this plastic zone can be identified by crack opening displacement (COD) load curves, which show slight crack closure for 35 mm $< a <$ 49 mm. This crack closure may cause a slightly lower stress intensity at the crack tip than predicted by the rearranged Eq. (2). A further detailed analysis of crack closure effects is part of a subsequent study reported in the future.

The overall excellent agreement of the 'experimental LSP simulation' of the unpeened material with the FCP experiments for the peened material validates ΔK_{cd} and R_{cd} as the most important crack-driving

[7] As tensile residual stresses are present for $a < x_1$, K^*_{res} corresponds to K_{res}.

quantities and thus the proposed multi-step simulation strategy. It is concluded that the used simplifications of the simulation approach are applicable during the calculation of these crack-driving quantities. Furthermore, the FCP behaviour can be explained by the influence of macroscopic residual stresses exclusively.

6. Conclusion

The objective of this work is the prediction of the FCP rate in AA2024-T3 with 4.8 mm thickness under the influence of LSP-generated residual stresses. A sequential FE simulation strategy is proposed and applied, allowing the prediction of the FCP rate based on the surface pressure caused by the LSP treatment and the applied laser pulse pattern. The simulation strategy is split into four main steps: (i) LSP process simulation; (ii) plastic strain transfer; (iii) FCP simulation; and (iv) calculation of FCP rate. The first step involves an LSP process simulation to predict the resulting plastic strains with a minimum number of laser shots. The second step includes the plastic strain transfer from the LSP process simulation to an extended area within C(T) specimens based on an eigenstrain approach. In the third step, the prediction of the crack-driving stress intensity factors at the crack tip is performed. ΔK_{cd} and R_{cd} are calculated as crack-driving quantities and are used as inputs for the fourth step, where FCP equations are used to predict the FCP rate. The material parameters of the FCP equations were identified by experiments for unpeened material only. Hence, no fitting between simulations and experiments of the peened specimen is required in this step. The predicted and measured FCP rates are in good agreement.

The application of the eigenstrain method is validated with residual stress measurements. Especially the non-equibiaxiality of the residual stresses is predicted precisely. The eigenstrain approach allows the reduction of the simulated laser impacts of the LSP process simulation to a minimum, since the predicted plastic strains of the LSP process simulation are extended to a large area of the C(T) specimen. The number of laser impacts to be simulated is reduced from approximately 530 (laser pulses used during the experiments) to 36 (laser pulses simulated in the LSP-process model), corresponding to a reduction of 93.2% of the laser pulses for the current example. This leads to a significant reduction in computational costs for this approach.

The assumed main crack-driving quantities ΔK_{cd} and R_{cd}, determined numerically, were applied to an unpeened specimen to determine the influence of any other effect on the FCP behaviour. Based on the excellent agreement between the peened specimen and this performed experiment, ΔK_{cd} and R_{cd} are identified as the significant crack-driving quantities for FCP growth within a C(T) specimen for the used process parameters. Hence, the FCP can be explained by the macroscopic residual stresses exclusively. Further effects are deduced to be negligible for the fatigue behaviour in the current case.

Based on the performed analysis, the following simplifications and assumptions for the FCP rate prediction are found to be valid:

- Residual stress relaxation due to cyclic loading and the generation of a plastic wake behind the crack tip are neglected.
- Plastic strains were averaged, leading to a homogeneous residual stress distribution inside the peened area. This simplifies the predicted residual stress field after the LSP process simulation, which shows high fluctuations. In addition, the influence of the clad layer is neglected based on residual stress predictions.
- Pure mode I loading at the crack tip and plane stress conditions are considered during the calculation of the stress intensity factors using CCT.
- A straight crack path and plane crack edges are assumed.

References

[1] Pacchinoe M, Telgkamp J. Challenges of the metallic fuselage. In: Proceedings 25th ICAS, Hamburg, Germany; 2006.
[2] Reid L. Sustaining an aging aircraft fleet with practical life enhancement methods. Technical Report. DTIC Document; 2003.
[3] Hombergsmeier E, Holzinger V, Heckenberger UC. Fatigue crack retardation in LSP and SP treated aluminium specimens. Adv Mater Res 2014;891:986–91.
[4] Hatamleh O, Lyons J, Forman R. Laser and shot peening effects on fatigue crack growth in friction stir welded 7075-T7351 aluminum alloy joints. Int J Fatigue 2007;29:421–34.
[5] Liljedahl C, Brouard J, Zanellato O, Lin J, Tan M, Ganguly S, et al. Weld residual stress effects on fatigue crack growth behaviour of aluminium alloy 2024-T351. Int J Fatigue 2009;31:1081–8.
[6] Liljedahl C, Zanellato O, Fitzpatrick M, Lin J, Edwards L. The effect of weld residual stresses and their re-distribution with crack growth during fatigue under constant amplitude loading. Int J Fatigue 2010;32:735–43.
[7] Servetti G, Zhang X. Predicting fatigue crack growth rate in a welded butt joint: the role of effective R ratio in accounting for residual stress effect. Eng Fract Mech 2009;76:1589–602.
[8] Irving P, Ma YE, Zhang X, Servetti G, Williams S, Moore G, et al. Control of crack growth rates and crack trajectories for enhanced fail safety and damage tolerance in welded aircraft structures. International committee on aeronautical fatigue and structural integrity 2009, bridging the gap between theory and operational practice. Springer; 2009. p. 387–405.
[9] Paris P, Erdogan F. A critical analysis of crack propagation laws. J Basic Eng 1963;85:528–33.
[10] Walker K. The effect of stress ratio during crack propagation and fatigue for 2024-T3 and 7075-T6 aluminum. In: Effects of environment and complex load history on fatigue life. ASTM International; 1970.
[11] Schnubel D, Huber N. Retardation of fatigue crack growth in aircraft aluminium alloys via laser heating–numerical prediction of fatigue crack growth. Comput Mater Sci 2012;65:461–9.
[12] NASGRO® Consortium and others. Fatigue crack growth computer program NASGRO® version 3.0. User manual, JSC-22267B. NASA Technical report; 2001.
[13] Elber W. The significance of fatigue crack closure. In: Damage tolerance in aircraft structures. ASTM International; 1971.
[14] Parker A. Stress intensity factors, crack profiles, and fatigue crack growth rates in residual stress fields. In: Residual stress effects in fatigue. ASTM International; 1982.
[15] Itoh Y, Suruga S, Kashiwaya H. Prediction of fatigue crack growth rate in welding residual stress field. Eng Fract Mech 1989;33:397–407.
[16] Bao R, Zhang X, Yahaya NA. Evaluating stress intensity factors due to weld residual stresses by the weight function and finite element methods. Eng Fract Mech 2010;77:2550–66.
[17] Schnubel D, Huber N. The influence of crack face contact on the prediction of fatigue crack propagation in residual stress fields. Eng Fract Mech 2012;84:15–24.
[18] Brockman RA, Braisted WR, Olson SE, Tenaglia RD, Clauer AH, Langer K, et al. Prediction and characterization of residual stresses from laser shock peening. Int J Fatigue 2012;36:96–108.
[19] Vaidya W, Staron P, Horstmann M. Fatigue crack propagation into the residual stress field along and perpendicular to laser beam butt-weld in aluminium alloy AA6056. Fatigue Fract Eng Mater Struct 2012;35:399–411.
[20] Dursun T, Soutis C. Recent developments in advanced aircraft aluminium alloys. Mater Des 2014;56:862–71.
[21] Verma B, Atkinson J, Kumar M. Study of fatigue behaviour of 7475 aluminium alloy. Bull Mater Sci 2001;24:231–6.
[22] Askar'yan G, Moroz E. Pressure on evaporation of matter in a radiation beam. Soviet J Exp Theor Phys 1963;16:1638.
[23] Fairand B, Wilcox B, Gallagher W, Williams D. Laser shock-induced microstructural and mechanical property changes in 7075 aluminum. J Appl Phys 1972;43:3893–5.
[24] Peyre P, Fabbro R, Merrien P, Lieurade H. Laser shock processing of aluminium alloys. Application to high cycle fatigue behaviour. Mater Sci Eng: A 1996;210:102–13.
[25] Clauer AH, Lahrman DF. Laser shock processing as a surface enhancement process. Key Eng Mater 2001;197:121–44.
[26] Sticchi M, Schnubel D, Kashaev N, Huber N. Review of residual stress modification techniques for extending the fatigue life of metallic aircraft components. Appl Mech Rev 2015;67:010801.
[27] Fabbro R, Fournier J, Ballard P, Devaux D, Virmont J. Physical study of laser-produced plasma in confined geometry. J Appl Phys 1990;68:775–84.
[28] Peyre P, Fabbro R. Laser shock processing: a review of the physics and applications. Opt Quant Electron 1995;27:1213–29.
[29] Peyre P, Berthe L, Scherpereel X, Fabbro R. Laser-shock processing of aluminium-coated 55C1 steel in water-confinement regime, characterization and application to high-cycle fatigue behaviour. J Mater Sci 1998;33:1421–9.
[30] Bhamare S, Ramakrishnan G, Mannava SR, Langer K, Vasudevan VK, Qian D. Simulation-based optimization of laser shock peening process for improved bending fatigue life of Ti–6Al–2Sn–4Zr–2Mo alloy. Surface Coat Technol 2013;232:464–74.
[31] Spradlin TJ, Grandhi RV, Langer K. Experimental validation of simulated fatigue life estimates in laser-peened aluminum. Int J Struct Integr 2011;2:74–86.
[32] Achintha M, Nowell D. Eigenstrain modelling of residual stresses generated by laser shock peening. J Mater Process Technol 2011;211:1091–101.
[33] Keller S, Chupakhin S, Staron P, Maawad E, Kashaev N, Klusemann B. Experimental and numerical investigation of residual stresses in laser shock peened AA2198. J Mater Process Technol 2018;255:294–307.
[34] Amarchinta HK, Grandhi RV, Clauer AH, Langer K, Stargel DS. Simulation of residual stress induced by a laser peening process through inverse optimization of material models. J Mater Process Technol 2010;210:1997–2006.
[35] Johnson GR. A constitutive model and data for metals subjected to large strains,

high strain rates and high temperatures. In: Proceedings of the 7th international symposium on ballistics, The Hague, Netherlands; 1983.
[36] Steinzig M, Ponslet E. Residual stress measurement using the hole drilling method and laser speckle interferometry: Part I. Exp Tech 2003;27:43–6.
[37] Ponslet E, Steinzig M. Residual stress measurement using the hole drilling method and laser speckle interferometry. Part II: Analysis technique. Exp Tech 2003;27:17–21.
[38] Ponslet E, Steinzig M. Technology application series: Residual stress measurement using the hole drilling method and laser speckle interferometry - Part III: Analysis technique. Exp Tech 2003;27:45–8.
[39] Schajer GS, Steinzig M. Full-field calculation of hole drilling residual stresses from electronic speckle pattern interferometry data. Exp Mech 2005;45:526.
[40] Rooke DP, Cartwright DJ. Compendium of stress intensity factors. Procurement Executive, Ministry of Defence. H.M.S.O. 1976, 330 p(Book); 1976.
[41] Newman JJ. A crack opening stress equation for fatigue crack growth. Int J Fract 1984;24:R131–5.
[42] Hill MR. Modeling of residual stress effects using eigenstrain. In: International conference on fracture 10, Honolulu (USA); 2001.
[43] Lei Y, O'dowd N, Webster G. Fracture mechanics analysis of a crack in a residual stress field. Int J Fract 2000;106:195–216.
[44] Sticchi M, Staron P, Sano Y, Meixer M, Klaus M, Rebelo-Kornmeier J, et al. A parametric study of laser spot size and coverage on the laser shock peening induced residual stress in thin aluminium samples. J Eng 2015;13:97–105.
[45] Krueger R. Virtual crack closure technique: history, approach, and applications. Appl Mech Rev 2004;57:109–43.
[46] Mann T. The influence of mean stress on fatigue crack propagation in aluminium alloys. Int J Fatigue 2007;29:1393–401.